

Quantifying the local tissue volume and composition in individual brains with magnetic resonance imaging

Aviv Mezer¹, Jason D Yeatman¹, Nikola Stikov², Kendrick N Kay¹, Nam-Joon Cho^{3,4}, Robert F Dougherty⁵, Michael L Perry¹, Josef Parvizi⁶, Le H Hua⁶, Kim Butts-Pauly⁷ & Brian A Wandell^{1,5}

Here, we describe a quantitative neuroimaging method to estimate the macromolecular tissue volume (MTV), a fundamental measure of brain anatomy. By making measurements over a range of field strengths and scan parameters, we tested the key assumptions and the robustness of the method. The measurements confirm that a consistent quantitative estimate of MTV can be obtained across a range of scanners. MTV estimates are sufficiently precise to enable a comparison between data obtained from an individual subject with control population data. We describe two applications. First, we show that MTV estimates can be combined with T1 and diffusion measurements to augment our understanding of the tissue properties. Second, we show that MTV provides a sensitive measure of disease status in individual patients with multiple sclerosis. The MTV maps are obtained using short clinically appropriate scans that can reveal how tissue changes influence behavior and cognition.

Magnetic resonance imaging (MRI) signals are often designed to reveal qualitative tissue contrast, but there are clinical and scientific advantages for designing quantitative MRI (qMRI) methods^{1–4}. Just as we can quantitatively measure body temperature or blood pressure, clinicians can use qMRI to quantitatively assess brain tissue. qMRI is well suited for clinical trial measurements at different sites and time points, and it is also critical for research of the neural and cellular bases of development, behavior and disease. Yet, current diagnostic practice is rarely based on qMRI owing to practical limitations (for example, long scan duration, low signal-to-noise ratio, low accuracy and unique nonclinical scan sequences).

Tissue volume measurement can be used to evaluate a variety of clinical disorders^{1,5–7}. However, the widely used methods, voxel-based morphometry⁸ and cortical thickness^{9,10}, are qualitative; they are derived from a statistical analysis of uncalibrated MRI images that depend on multiple biological factors, including regional brain size and shape, thickness of the cortex and myelination. Changes in these parameters reflect development across the lifespan and disease impairment and are correlated with behavior and cognition^{10–13}, but

the conclusions drawn from these analyses do not point to a specific biological property¹⁴.

We describe a quantitative neuroimaging method to estimate the brain MTV. Brain macromolecules are principally cell membranes and proteins; in white matter, approximately 50% are myelin sheaths¹⁵. Along with MTV, the method measures the protons observed longitudinal relaxation time constant (quantitative T1 map). T1 values depend on the MTV and the physicochemical environment of the macromolecules surfaces^{16–18}. We describe ways of combining MTV and T1 in order to measure the macromolecular composition. Further, we show that combining MTV with diffusion measurements provides insight about macroscopic tissue organization. We test the accuracy of these methods for individual clinical assessment across a range of MR scanners, field strengths, radiofrequency (RF) coils and time points. Finally, we describe measurements of white matter in individuals with multiple sclerosis.

RESULTS

Measurement of MTV

MTV quantifies the nonwater volume in each voxel, and the complementary volume is water. The amount of water in a voxel is estimated from the proton density (PD) signal. The PD values are proportional to the amount of water, with an unknown constant of proportionality. We approximated cerebrospinal fluid (CSF) voxels as entirely filled with water, and thus, for each voxel, the water volume fraction (WVF) is the ratio of the PD values in tissue to the PD values in CSF. We defined the voxel MTV fraction (MTVF) by the equation $MTVF = 1 - WVF$ (for glossary see **Supplementary Table 1**).

To estimate the voxel MTV, we first calculated instrumental biases from the data. The PD and T1 values were then derived from the signal equation of the spoiled-gradient-echo (spoiled-GE) clinical sequence^{17,19} (see Online Methods for the fully automatic post-processing technique that is implemented in the software we distribute (<https://github.com/mezera/mrQ>), which is summarized in the pipeline diagram in **Supplementary Figure 1**. The transmit-coil inhomogeneity was corrected by combining the spoiled-GE sequence with a set of unbiased spin-echo inversion-recovery scans (**Supplementary Fig. 2**). The receive-coil inhomogeneity was

¹Department of Psychology, Stanford University, Stanford, California, USA. ²Montreal Neurological Institute, McGill University, Montreal, Quebec, Canada.

³Department of Chemical Engineering, Stanford University, Stanford, California, USA. ⁴School of Materials Science and Engineering, Nanyang Technological University, Singapore, Singapore. ⁵Center for Cognitive and Neurobiological Imaging, Stanford University, Stanford, California, USA. ⁶Department of Neurology and Neurological Sciences, Stanford University, Stanford, California, USA. ⁷Department of Radiology, Stanford University, Stanford, California, USA. Correspondence should be addressed to A.M. (avivmezer@gmail.com).

Received 12 October 2012; accepted 5 February 2013; published online 3 November 2013; doi:10.1038/nm.3390

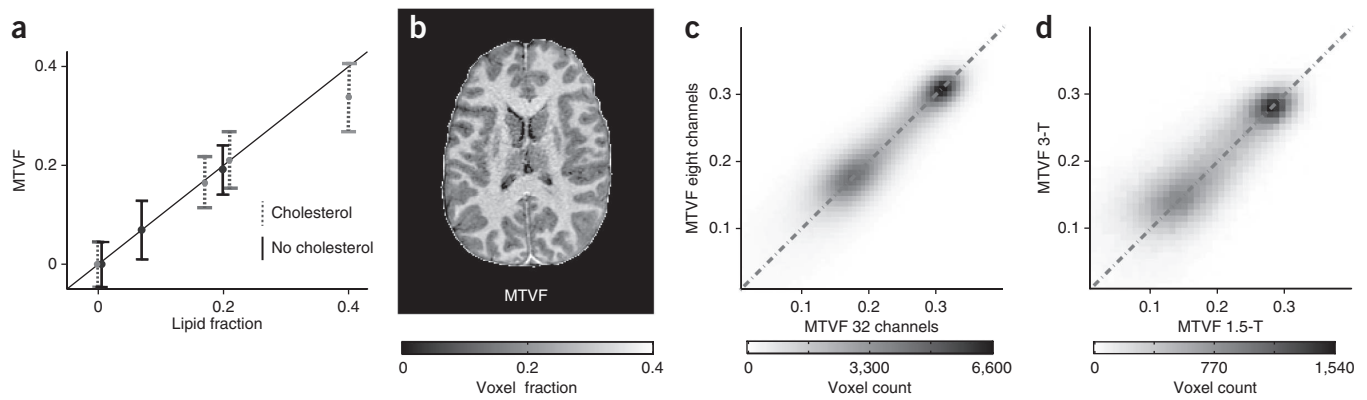


Figure 1 Assessment of MTV fraction accuracy and reliability. **(a)** The MTV fraction (MTVF) was measured using two types of lipid mixtures: one with cholesterol (30% weight, gray dotted lines) and one without cholesterol (black lines) embedded in the lipid membranes. The lipid fraction and estimated MTV are both given in fraction of the voxel. The values are close to the identity line, which shows that MTV can be accurately quantified. Data are expressed as means \pm s.d., and the average s.d. is 0.053. **(b)** An axial brain slice showing an MTV map. The different brain MTV fraction values are plotted using the gray scale shown in the bottom of the map. **(c)** Comparison of MTV values in the gray and white matter measured twice in the same subject with two different RF coils (one eight-channel and one 32-channel) ($R^2 = 0.84$). The two dark regions represent MTVF values from the gray (lower) and white (higher) matter. The number of voxels for each MTVF value is given by the light-to-dark voxel count scale. **(d)** Comparison of MTVF values in the same brain measured in a 1.5-T and 3.0-T scanner ($R^2 = 0.67$). The scans in **c** were acquired on the same day; 6 months passed between the two scans compared in **d**.

estimated using the logic developed for parallel imaging algorithms. The key idea was to separate the coil effects from the brain signal using data from the individual coils (**Supplementary Fig. 3**). The data acquisition was straightforward, relying on vendor-supplied sequences, and took about 12 min for clinical (2 mm³) and 25 min for submillimeter resolutions.

Validating MTV accuracy and reliability

In the first experiment, we estimated MTV in phantoms with controlled volumes. We mixed phosphatidylcholine lipid, cholesterol and water with different volume levels. The MTV reliably quantified the lipid volume (**Fig. 1a**). The accuracy of the MTV estimates showed that the coil inhomogeneities that influence the raw measurements were corrected for the MTV values. The MTV value was estimated independently of the cholesterol content. Hence, MTV is different from T1, which changes substantially when cholesterol is present^{20,21}.

Next, we evaluated the instrumental independence of the MTV estimates (**Fig. 1b–d**). We compared MTV estimates from the same brain obtained with different coils at 3 Tesla (3 T) and from 1.5-T and 3.0-T magnets as well at different time points. Along with MTV, we obtained the observed T1 map. We tested the stability of these T1 maps across different field strengths, coils, repetition time (TR), echo time (TE) and flip-angle parameters (**Supplementary Figs. 2 and 4–6**). The consistency of both maps across the wide variety of measurement conditions validates the accuracy of the methods for removing coil bias and the model assumptions (for further discussion see **Supplementary Discussion**).

Variation in MTV between brain structures

The MTV values differed between parts of the brain; MTV values are summarized for three large brain regions ($n = 16$) in **Figure 2**. These values are in agreement with postmortem measurements¹. The summary measurements show that the MTV values averaged across these large brain regions are extremely similar between subjects. The difference between gray and white matter is substantial (35%), but the thalamus region values are close to the gray matter values. These comparisons are spatially coarse; a more detailed example for the corpus callosum (CC) is given below.

The CC comprises a set of tracts that carry signals between different functional regions of cortex. Histological and MRI measurements show that along the anterior-posterior axis of the CC, axons differ in size, in number^{22,23} and potentially also in axonal packing density²⁴. We compared the MTV values in distinct zones within the CC segments that contain axons with terminals in different cortical regions (**Fig. 3a**). Using tractography, we identified three CC zones: the body, the splenium and the genu-rostrum. These zones include axons from the motor, visual and orbitofrontal cortices, respectively.

The mean MTV values in these three regions (**Fig. 3b**) are smallest in the body where axonal diameters are largest²², larger in the splenium and largest in the genu-rostrum. The MTV differences are quite substantial: the body is separated by about 10 s.e.m. from the genu-rostrum and by about 8 s.e.m. from splenium.

Combining MTV and diffusion imaging

Diffusion-weighted imaging measures the intravoxel water diffusion in multiple orientations. The diffusion orientation distribution function is clinically modeled by a tensor, which is summarized by its fractional anisotropy (FA)²⁵. The FA value combines a range of

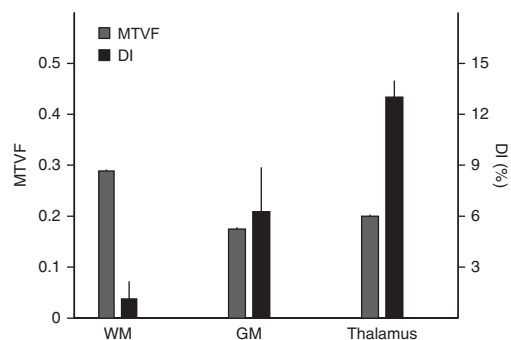


Figure 2 The MTVF and dissimilarity index (DI) in different brain regions. The mean MTVF (left axis) and DI (right axis) are averages from three large regions of interest (ROI, $n = 16$) defined by FreeSurfer⁹. The voxels within each ROI that border other regions were excluded. Data are expressed as mean \pm s.e.m. WM, white matter; GM, gray matter.

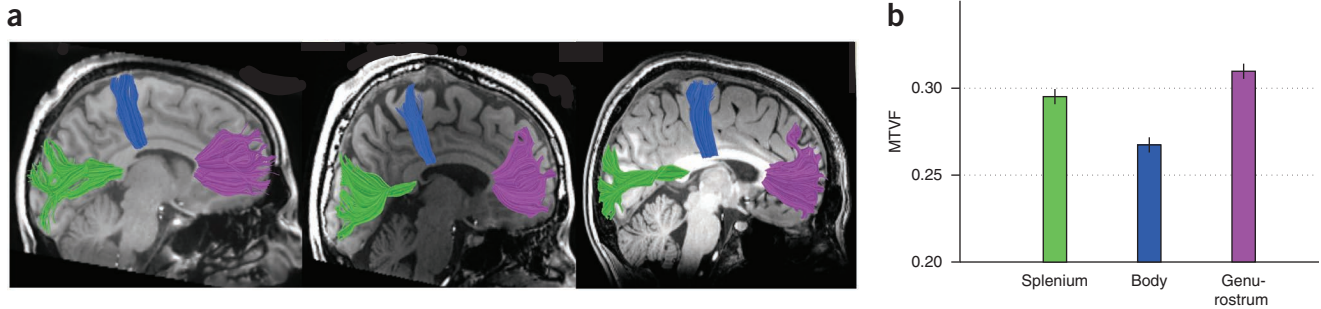


Figure 3 The mean MTVF values near the midline of three callosal tracts. (a) Midsagittal T1-weighted images are shown from three subjects. Three callosal fiber tracts estimated using deterministic DTI tractography overlay the images: motor fibers, blue; visual fibers, green; orbitofrontal fibers, purple. The tracts segment the CC into three distinct zones: the body, the splenium and the genu-rostrum, respectively. (b) The mean MTVF values within a 5-mm portion of each tract on either side of the midsagittal plane ($n = 15$). The MTVF values in the body are considerably smaller than the MTVF values within the other regions, and the genu-rostrum values are the largest. Data are expressed as mean \pm s.e.m.

geometric and microstructural factors, and it would be valuable to distinguish between these biological factors^{26,27}. Hence, there is potential benefit of combining MTV and diffusion measurements to clarify the contributions of different tissue properties. To illustrate one benefit, we determined the MTV and FA values along the corticospinal tract (CST). We identified each subject's CST core fiber ($n = 15$) and measured the FA and MTV along the fiber²⁸. The FA value dropped substantially in the region where fibers from the CC pass through the CST, reducing fiber-direction coherence (Fig. 4a). This region is within the centrum semiovale, where there are known to be many crossing fibers²⁹. This drop in FA was consistent across all subjects (Fig. 4b). The MTV values, on the other hand, were constant along the CST (Fig. 4c). Notably, the crossing fibers did not considerably affect

the MTV. This example illustrates that FA and MTV values show the complementary aspects of the white matter tracts. Combining the two measurements helps discriminate between different mechanisms that influence FA. For example, if MTV and FA change together, we would be inclined to explain the change as one caused by an axon-packing difference. If MTV is constant but FA changes, we might explain the change as one caused by mechanisms such as differences in axon coherence.

The pattern of the data in Figure 4 is typical of another difference between diffusion and tissue property measures. The MTV s.d. between subject tracts was 30% greater than the difference within each subject's tract (7.5×10^{-4} between subjects compared to 1.1×10^{-3} within a subject). The situation was reversed for FA (9.8×10^{-2} compared to 4.6×10^{-2}). Therefore, MTV values, which are highly reliable across instruments and repetitions, may be a particularly useful measure to distinguish between individuals.

Combining MTV and T1 mapping

Brain T1 depends on both the density of macromolecules and the local physicochemical environment¹⁶⁻¹⁸. Consequently, there should be a relationship between the measured T1 and MTV values. Earlier work showed^{5,30} a linear relationship between $1/(1 - MTVF)$ and $1/T1$. We confirmed this relationship using the data from all of the white matter of individual subjects and provide a summary of

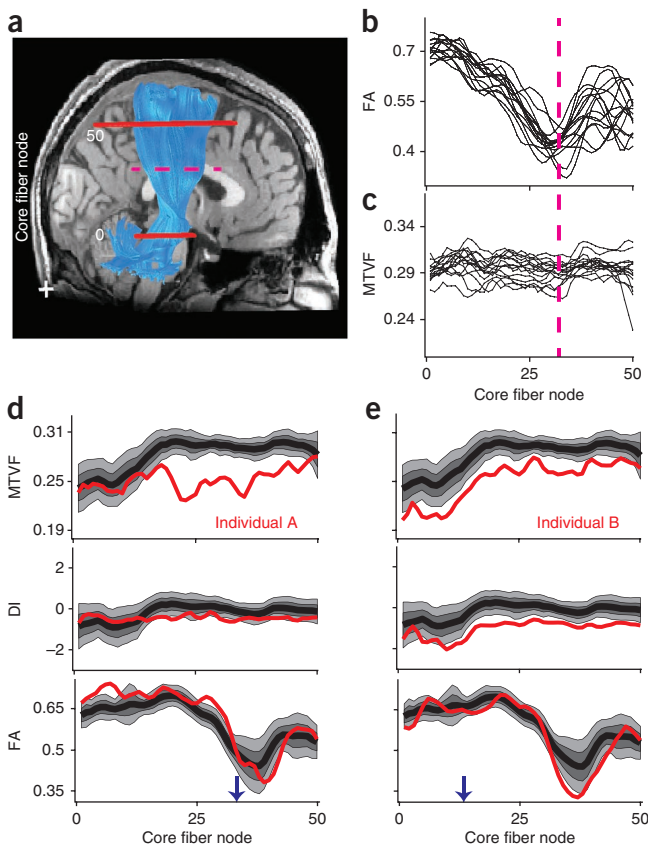


Figure 4 Corticospinal tract (CST) measurements in controls and two individuals with multiple sclerosis. (a) The estimated right CST (blue) is overlaid on a sagittal T1-weighted image. The two solid red lines show axial planes that designate the measurement region; the centroid of the tract (core fiber) is calculated and sampled into 50 nodes. The CST intersection with the callosal fibers is designated by the dashed fuschia line. (b,c) The curves show FA and MTVF values measured at different nodes along the CST from different control subjects ($n = 15$). The FA value, but not the MTVF value, declines in the region where the CST intersects callosal fibers (dashed fuschia line). (d) The MTVF, DI and FA values along the left CST in individual A with multiple sclerosis (red) are compared with the distribution of measurements from the controls. The black curve represents the control mean, and the lighter shades show the interquartile range and the 10th–90th percentile range. In individual A, the MTVF values are substantially below the control values in the superior portion of the CST. The DI and FA values are close to the control range throughout. The arrow indicates the core fiber node corresponding to the axial plane further analyzed in Supplementary Figure 12. (e) In individual B, the MTVF and the DI values are consistently below the distribution of control values. The CST region appears normal in the diagnostic images shown in Supplementary Figure 12.



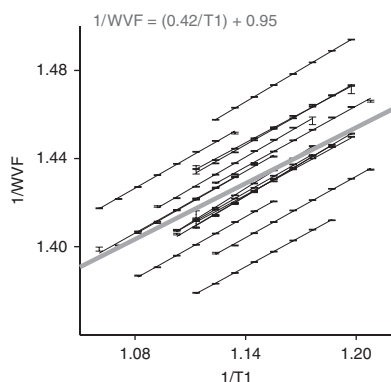


Figure 5 The relationship between T1 and WVF in white matter. The white matter R1 (1/T1) plotted against 1/WVF (water volume fraction (WVF = 1 – MTVF, $n = 16$). The R1 values are pooled into bins separated by intervals of 0.05 s^{-1} . The mean number of voxels in each bin is $1.5 \times 10^5 \pm 5.5 \times 10^3$. Data from 16 individual subjects are fitted accurately by lines. Data are expressed as means \pm s.e.m. The linear fit combining data from all subjects is shown as a thick gray line, and the formula for that line is in the equation at the top of the figure.

the linear relationship based on the data from all subjects (Fig. 5). This average is given by equation (1):

$$\frac{1}{(1 - \text{MTVF})} = \frac{0.42}{T1} + 0.95 \quad (1)$$

The slope and intercept are close to the values reported elsewhere^{5,30}.

Whereas the linear relationship characterizes the main effect, deviations from the line contribute additional information about the local physicochemical environment. Earlier work showed that observed T1 depends on both the ensemble^{20,21} and compartmentalization of the macromolecules³¹. To measure the local physicochemical environment, we computed a dissimilarity index (DI) between the measured and predicted R1 = (1/T1) (equation (1)) using equation (2):

$$\text{DI} = 100 \times \frac{R1_{\text{measured}} - R1_{\text{predicted}}}{R1_{\text{measured}}} \quad (2)$$

If two voxels differ only in MTV and their physicochemical environment is equal, DI should be zero. Measured DI values differed substantially when we compared white matter, gray matter and thalamus (Fig. 2). For example, the gray matter and thalamus regions had similar MTV values (0.18–0.20), but the DI values differed by a substantial amount (6% in gray matter and 12% in thalamus). These measurements show that MTV within a single tissue class (white matter) predict the T1, but the same prediction does not extend to different brain tissue (gray matter and thalamus). Hence, comparing T1 and MTV values between tissues is informative about the local physicochemical environment of the macromolecules.

The DI measurement was based on the observed T1 without any assumption regarding the biophysical source. In the **Supplementary Discussion**, we review the T1 literature and develop a biophysical framework that explains the brain T1 value differences. The model develops a formula that transforms the MTV and T1 values (in seconds) to a tissue property, which we have named ‘the apparent volume of the interacting water protons’ (VIP). In a nutshell, this

model assumes that tissue T1 relaxation time may be explained by both the amount of the tissue-water interface and the water-surface interaction rate (SIR). This model assumes a fast exchange between proton pools and neglects effects of slow exchange. We analyzed the likely size of slow-exchange effects (**Supplementary Fig. 7**).

Adding cholesterol to a lipid mixture does not change the MTV estimate (Fig. 1); therefore, MTV is independent of the type of macromolecule. However, SIR does depend on the lipid cholesterol (**Supplementary Fig. 8**). Hence, SIR is dependent on the local physicochemical environments. SIR estimates are independent over a range of clinically relevant field strengths (0.5 T–3 T) (**Supplementary Fig. 9**).

Multiple sclerosis

A clinical application for MTV and T1 measurements is the identification and monitoring of brain tissue changes. Specifically, a reliable MRI approach for the assessment of demyelinating disorders such as multiple sclerosis has yet to be standardized^{32–34}. In clinical practice^{32–34}, lesions are typically monitored with conventional MR metrics that identify hyperintensities in T2-weighted images and/or gadolinium enhancement on T1-weighted images as markers of disease activity and hypointensities in T1-weighted images as markers of neuronal degeneration. Quantitative MTV measurement can be used to compare individual subjects with respect to control populations over time and across MRI centers and scanners, serving as a noninvasive biomarker for both disease monitoring and drug design. Other qMRI methods such as magnetization transfer (MT) and T2 mapping also detect lesions (see ref. 35). These protocols are not part of the current clinical assessment because of the long scan time required to achieve satisfactory resolution and reliability. The MTV is highly correlated with quantitative MT ($r = 0.9$) in white matter tracks and with T2 myelin water fraction ($r = 0.79$, additional details in **Supplementary Discussion** and **Supplementary Fig. 10**).

We compared the MTV, DI and FA levels of ten individuals with relapsing-remitting multiple sclerosis with the same measurements in a group of control subjects ($n = 16$). We observed reliable quantitative differences between individual patients and the controls in specific white matter tracts. We describe two individuals who both have CST tissue abnormalities (Fig. 4d,e; further examples in **Supplementary Fig. 11**). Both subjects had FA values in the CST within the normal range. In subject A, MTV values in the superior portion of the tract were below the control population distribution, whereas in subject B, the MTV values along the entire CST were below the control population distribution. The fluid-attenuated inversion-recovery (FLAIR) and T1-weighted diagnostic images (**Supplementary Fig. 12**) showed a localized abnormality for subject A, but the images appeared normal for subject B.

Multiple sclerosis postmortem histology shows both a reduction in macromolecular volume and a change in tissue characteristics³⁶. In both subjects, there was a reduction in the MTV, but only subject B showed a variation in DI, which suggests that there was also a change in the macromolecular tissue from that typical in white matter.

Thus, MTV measurements identify abnormal regions and quantify the size of these deviations in normal-appearing white matter, and DI measurements add information about changes in the tissue physicochemical environment.

DISCUSSION

The MR signal arises from protons that probe tissue properties at the nanometer scale³⁷. MTV is the most basic MR measurement and

assesses the volume of water and nonwater in each voxel. MR estimates derived by our methods were consistent across field strengths, coils and time and agreed with histology and with lipid phantoms, suggesting the method is accurate. Combining MTV with diffusion measurements distinguishes between variation in tissue orientation and tissue density, whereas combining MTV with T1 mapping informs us about variations in local physicochemical environments. We found tissue differences between brain regions and between individuals with multiple sclerosis and controls, bringing *in vivo* human imaging a step closer to helping us understand the biochemistry and biophysics of the underlying brain tissue.

Contrast measurements are sufficient for investigations that aim to identify only the location of unusual tissue. The next goal in MRI is to quantitatively assess specific tissue properties. This goal is challenging because MR scanners generally operate with incomplete calibrations. Some procedures in the literature propose to remove bias by taking the ratio of two images with a common bias (for example, T1 and T2 (ref. 38)) or by calculating a MT ratio¹. Other procedures reduce biases through statistical smoothing^{39,40} or through combining data sets from multiple subjects^{8,9}. Our method goes beyond these procedures by using absolute calibration procedures to eliminate both receive-RF and excite-RF coil inhomogeneities.

The current measurements are limited by the same technical challenges that limit imaging of all large volumes: imperfections in the main field and coil corrections both bias the estimates. Further, deviations from the main fitting assumptions might limit the accuracy of the estimates. We assume that the images are free from T2* weighting (see Online Methods), given the chosen TE. Our confidence in this assumption comes from the agreement of the MTV values with prior measurements using different methods and between our measurements in different magnetic fields. To explain the T1 properties of different tissues, we suggest a biophysical model in the **Supplementary Discussion**; however, further investigation is needed to establish the biophysical interpretation of the DI measurements.

MTV and T1 mapping makes use of a short straightforward clinical sequence supplied by most MR scanners. The acquisition time is about 12 min for clinically relevant resolution (2 mm³) and 25 min for submillimeter resolution. These computations use simple and robust formulas that derive membrane and macromolecular properties obtain from high-quality signal-to-noise ratio and spatial resolution, as are shown by the spoiled-GE images (**Fig. 1b**). Together, these advantages make it possible to use the MTV and T1 methods for scientific and clinical applications by facilitating comparison of data across multiple sites and enabling comparisons between individual participants or patient to a control population or in the same individual over time.

METHODS

Methods and any associated references are available in the [online version of the paper](#).

Note: Any Supplementary Information and Source Data files are available in the online version of the paper.

ACKNOWLEDGMENTS

We acknowledge J. Barral, M. Gutman, H. Horiguchi, I. Levesque, A. Sherbondy and A. Takahashi for helpful advice and feedback. We thank S. Phipps, I. Levesque and A. Kerr for help in data analysis and acquisition. This work was supported by the US National Institutes of Health research grants RO1-EY15000 and NSF grant BCS-1228397. A.M. is the recipient of support from the Human Frontier Science Program and a Jewish Community Federation Program Machiah Foundation

Fellowship. N.-J.C. is the recipient of support from the Singapore National Research Foundation (NRF-NRFF2011-01).

AUTHOR CONTRIBUTIONS

A.M. and B.A.W. developed the method, wrote the manuscript and prepared the figures. J.D.Y., N.S., M.L.P., R.F.D., K.B.-P. and A.M. obtained the data. N.-J.C. provided the lipid phantoms. N.S., R.F.D., K.N.K. and A.M. developed analysis tools. J.P. and L.H.H. diagnosed the patient with multiple sclerosis and enabled those scans. A.M. and J.D.Y. developed the diffusion methods and applications. B.A.W. provided equipment and administered the experiment. All authors reviewed the manuscript.

COMPETING FINANCIAL INTERESTS

The authors declare competing financial interests: details are available in the [online version of the paper](#).

Reprints and permissions information is available online at <http://www.nature.com/reprints/index.html>.

- Tofts, P. *Quantitative MRI of the Brain Measuring Changes Caused by Disease* (John Wiley & Sons, Chichester, West Sussex; Hoboken, NJ, 2003).
- Laule, C. *et al.* Magnetic resonance imaging of myelin. *Neurotherapeutics* **4**, 460–484 (2007).
- Deoni, S.C. Magnetic resonance relaxation and quantitative measurement in the brain. *Methods Mol. Biol.* **711**, 65–108 (2011).
- Alexander, A.L. *et al.* Characterization of cerebral white matter properties using quantitative magnetic resonance imaging at 1.5T. *Brain Connect.* **1**, 423–426 (2011).
- Fatouros, P.P. & Marmarou, A. Use of magnetic resonance imaging for *in vivo* measurements of water content in human brain: method and normal values. *J. Neurosurg.* **90**, 109–115 (1999).
- Laule, C. *et al.* Water content and myelin water fraction in multiple sclerosis. A T2 relaxation study. *J. Neurol.* **251**, 284–293 (2004).
- Neeb, H., Zilles, K. & Shah, N.J. A new method for fast quantitative mapping of absolute water content *in vivo*. *Neuroimage* **31**, 1156–1168 (2006).
- Ashburner, J. & Friston, K.J. Voxel-based morphometry—the methods. *Neuroimage* **11**, 805–821 (2000).
- Fischl, B. & Dale, A.M. Measuring the thickness of the human cerebral cortex from magnetic resonance images. *Proc. Natl. Acad. Sci. USA* **97**, 11050–11055 (2000).
- Gogtay, N. *et al.* Dynamic mapping of human cortical development during childhood through early adulthood. *Proc. Natl. Acad. Sci. USA* **101**, 8174–8179 (2004).
- Kakeda, S. & Korogi, Y. The efficacy of a voxel-based morphometry on the analysis of imaging in schizophrenia, temporal lobe epilepsy, and Alzheimer's disease/mild cognitive impairment: a review. *Neuroradiology* **52**, 711–721 (2010).
- Kanai, R. & Rees, G. The structural basis of inter-individual differences in human behaviour and cognition. *Nat. Rev. Neurosci.* **12**, 231–242 (2011).
- May, A. Experience-dependent structural plasticity in the adult human brain. *Trends Cogn. Sci.* **15**, 475–482 (2011).
- Thomas, C. & Baker, C.I. Remodeling human cortex through training: comment on May. *Trends Cogn. Sci.* **16**, 96–97 (2012).
- Norton, W.T. & Autilio, L.A. The lipid composition of purified bovine brain myelin. *J. Neurochem.* **13**, 213–222 (1966).
- Bottomley, P.A., Foster, T.H., Argersinger, R.E. & Pfeifer, L.M. A review of normal tissue hydrogen NMR relaxation times and relaxation mechanisms from 1–100 MHz: dependence on tissue type, NMR frequency, temperature, species, excision, and age. *Med. Phys.* **11**, 425–448 (1984).
- Mansfield, P. & Morris, P.G. *NMR Imaging in Biomedicine* (Academic Press, London, 1982).
- Rooney, W.D. *et al.* Magnetic field and tissue dependencies of human brain longitudinal 1H2O relaxation *in vivo*. *Magn. Reson. Med.* **57**, 308–318 (2007).
- Fram, E.K. *et al.* Rapid calculation of T1 using variable flip angle gradient refocused imaging. *Magn. Reson. Imaging* **5**, 201–208 (1987).
- Koenig, S.H. Cholesterol of myelin is the determinant of gray-white contrast in MRI of brain. *Magn. Reson. Med.* **20**, 285–291 (1991).
- Kucharczyk, W., Macdonald, P.M., Stanisz, G.J. & Henkelman, R.M. Relaxivity and magnetization transfer of white matter lipids at MR imaging: importance of cerebroside and pH. *Radiology* **192**, 521–529 (1994).
- Abowitz, F., Scheibel, A.B., Fisher, R.S. & Zaidel, E. Fiber composition of the human corpus callosum. *Brain Res.* **598**, 143–153 (1992).
- Barazany, D., Basser, P.J. & Assaf, Y. *In vivo* measurement of axon diameter distribution in the corpus callosum of rat brain. *Brain* **132**, 1210–1220 (2009).
- Stikov, N. *et al.* Bound pool fractions complement diffusion measures to describe white matter micro and macrostructure. *Neuroimage* **54**, 1112–1121 (2011).
- Alexander, A.L., Lee, J.E., Lazar, M. & Field, A.S. Diffusion tensor imaging of the brain. *Neurotherapeutics* **4**, 316–329 (2007).
- Beaulieu, C. The basis of anisotropic water diffusion in the nervous system—a technical review. *NMR Biomed.* **15**, 435–455 (2002).
- Paus, T. Growth of white matter in the adolescent brain: myelin or axon? *Brain Cogn.* **72**, 26–35 (2010).



28. Yeatman, J.D., Dougherty, R.F., Myall, N.J., Wandell, B.A. & Feldman, H.M. Tract profiles of white matter properties: automating fiber-tract quantification. *PLoS ONE* **7**, e49790 (2012).
29. Wedeen, V.J. *et al.* Diffusion spectrum magnetic resonance imaging (DSI) tractography of crossing fibers. *Neuroimage* **41**, 1267–1277 (2008).
30. Gelman, N., Ewing, J.R., Gorell, J.M., Spickler, E.M. & Solomon, E.G. Interregional variation of longitudinal relaxation rates in human brain at 3.0 T: relation to estimated iron and water contents. *Magn. Reson. Med.* **45**, 71–79 (2001).
31. Does, M.D. & Gore, J.C. Compartmental study of T(1) and T(2) in rat brain and trigeminal nerve *in vivo*. *Magn. Reson. Med.* **47**, 274–283 (2002).
32. Filippi, M. & Rocca, M.A. MR imaging of multiple sclerosis. *Radiology* **259**, 659–681 (2011).
33. Lövblad, K.O. *et al.* MR imaging in multiple sclerosis: review and recommendations for current practice. *AJNR Am. J. Neuroradiol.* **31**, 983–989 (2010).
34. Poloni, G., Minagar, A., Haacke, E.M. & Zivadinov, R. Recent developments in imaging of multiple sclerosis. *Neurologist* **17**, 185–204 (2011).
35. MacKay, A.L. *et al.* MR relaxation in multiple sclerosis. *Neuroimaging Clin. N. Am.* **19**, 1–26 (2009).
36. Popescu, B.F. & Lucchinetti, C.F. Pathology of demyelinating diseases. *Annu. Rev. Pathol.* **7**, 185–217 (2012).
37. Le Bihan, D. *et al.* Diffusion tensor imaging: concepts and applications. *J. Magn. Reson. Imaging* **13**, 534–546 (2001).
38. Glasser, M.F. & Van Essen, D.C. Mapping human cortical areas *in vivo* based on myelin content as revealed by T1- and T2-weighted MRI. *J. Neurosci.* **31**, 11597–11616 (2011).
39. Noterdaeme, O., Anderson, M., Gleeson, F. & Brady, S.M. Intensity correction with a pair of spoiled gradient recalled echo images. *Phys. Med. Biol.* **54**, 3473–3489 (2009).
40. Volz, S., Noth, U. & Deichmann, R. Correction of systematic errors in quantitative proton density mapping. *Magn. Reson. Med.* **68**, 74–85 (2012).

ONLINE METHODS

Lipids. Phantom construction. Large multilamellar vesicles (referred to hereafter as vesicles) consisting of L- α -phosphatidylcholine (Egg PC from soy extract, Avanti Polar Lipids, Alabaster, USA) with or without cholesterol were prepared by the sonication method. For all the analytical phantom measurements described here, we used a 10-mM PBS buffer solution (pH 7.5) with 150 mM NaCl. All solutions were prepared in 18.2 M Ω cm Milli-Q water (MilliPore, Oregon, USA). Lipid films were first prepared by drying the as-supplied lipids dissolved in chloroform under a gentle stream of nitrogen vapor at room temperature. The resulting lipid film was then stored under vacuum overnight to remove residual chloroform. Vesicles were prepared by swelling the lipid film in an aqueous solution followed by vortexing periodically for 10 min. The resulting vesicle solution was next sonicated with a probe-tip sonicator in order to produce uniform lipids solubility. Vesicles were generally used within 3 d of preparation. The mixtures were made with different lipid concentrations (see Fig. 1a). To calculate the lipid mixture volume, we determined the number of lipid molecules based on the molecular mass and volume (~1875 Å³) of a single lipid^{41–43}. For the mixture with cholesterol, we assume that the cholesterol volume is negligible, according to the free space theory⁴⁴. The different vesicle mixtures were poured into 3-ml cuvettes and glued to a plastic vessel. The vessel was filled with PBS buffer and sealed.

Magnetic resonance image acquisition. Data were obtained using a 1.5-T GE Signa MRI scanner. Spoiled-GE images were acquired with parameters similar to those used with human subjects (see below). The data processing was identical to the human MR data processing with two exceptions. First, the coil biases were estimated by a single set of three-dimensional (3D) second-order polynomial approximate over homogenous region (the vessel was filled with PBS). Second, the receive-coil inhomogeneity correction was scaled so that the water fraction (WF) of the PBS region was 1. The transmit-coil inhomogeneity correction was scaled so that the T1 of the PBS region was equal to the T1 of water at room temperature.

Human anatomical mapping. Subjects. Human measurements were performed on 16 healthy adult volunteers (10 female). In addition, ten volunteers with relapsing remitting multiple sclerosis (diagnosed based on revised McDonald criteria⁴⁵). The disease duration was 2–17 years with Expanded Disability Status scale values of <3.0 (ref. 46). All patients were on disease-modifying treatments (two on natalizumab, one on glatiramer acetate and seven on interferon β -1a) and free of steroids for at least 3 months at time of MR imaging. All studies were performed with the informed written consent of subjects. The Stanford University Institutional Review Board approved all procedures for medical research involving human subjects.

Magnetic resonance image acquisition. Data were obtained from five MR scanners: a 0.5-T GE-Signa SP ($n = 2$), two different 1.5-T GE-Signa ($n = 4$) and two different 3-T GE Signa ($n = 26$) MRI scanners. At 1.5 T, we used two different eight-channel receive-only head coils. At 3 T, in one magnet we used an eight-channel receive-only head coil and in the other we used a 32-channel receive-only head coil.

The quantitative T1 and MTV parameters were measured from spoiled-GE images acquired with different flip angles ($\alpha = 4^\circ, 10^\circ, 20^\circ$ and 30° , TR = 20 ms, TE = 2.4 ms). The scan resolutions at different field strengths were 0.5 T, $1.5 \times 1.5 \times 3$ mm³; 1.5 T, 1.5 mm³; 3 T, 1 mm³.

For T1 calibration, all subjects measured at 1.5 T and 3 T were also scanned using spin-echo inversion recovery with an echo-planar imaging (EPI) readout (SEIR-epi). This scan was done with a slab-inversion pulse and spatial-spectral fat suppression. For SEIR-epi, the TR was 3 s at 3 T and 2.5 s at 1.5 T. The echo time was set to minimum full; inversion times were 50, 400, 1,200 and 2,400 ms. We used 2-mm² in-plane resolution with a slice thickness of 4 mm. The EPI readout was performed using 2 \times acceleration at 3 T and no acceleration at 1.5 T.

To enable the use of post-scan calibration (below), we made sure that the manufacturer's pre-scan was performed only for the first scan. We ensured that these parameters were used for the remaining scans.

We released the analysis below as open-source MATLAB code (<https://github.com/mezera/mrQ>). An example data set can be found at <http://purl.stanford.edu/qh816pc3429>.

T1 mapping–transmit-coil inhomogeneity correction. The MTV values are estimated from measures of two fundamental MR maps: T1 and proton density (PD).

T1 and PD can be derived from a set of spoiled-GE images. The images signal (S) (equation (3))^{17,19} depends on three tissue-related MR constants, observed T1 and T2* relaxation times and PD. The equation also depends on four acquisition parameters: TR, TE, flip angle (α) and coil inhomogeneity.

$$S(\alpha) = M_0 \sin(\alpha) \left(\frac{1 - e^{-\frac{TR}{T1}}}{1 - \cos(\alpha)e^{-\frac{TR}{T1}}} \right) \quad (3)$$

The M_0 term combines g , a scale factor that characterizes receive-coil inhomogeneity gain, arbitrary instrument scaling, PD and the T2* decay constant (equation (4)).

$$M_0 = g \times PD \times e^{-\frac{TE}{T2^*}} \approx g \times PD \quad (4)$$

In principle, T1 and M_0 can be estimated by collecting measurements with at least two flip angles. In practice, the receive-coil and the transmit-coil are not perfectly calibrated. The receive-coil imperfection influences only the M_0 term, whereas the transmit-coil imperfection prevents us from knowing the true α at each brain voxel, which results in erroneous estimates of both T1 and M_0 . Consequently, we must estimate both transmit- and receive-coil inhomogeneity to derive the T1 and PD maps accurately.

Our strategy to overcome the transmit-coil calibration errors is as follows. We first use SEIR-epi to measure an unbiased low-resolution T1 map of the whole brain. We calculate T1 from SEIR data using the method described by Barrel *et al.*⁴⁷. We then align the T1 data with a matched low-resolution representation of the spoiled-GE data. From the T1 and several flip-angle spoiled-GE values, we use a nonlinear least-squares (NLS) solver and estimate the transmit-coil inhomogeneity and M_0 (equation (3)). Next we interpolate the low-resolution transmit-coil inhomogeneity data to the resolution of the original spoiled-GE measurements. We assume that the transmit-coil inhomogeneities are smooth and can be estimated by local regressions of hyperplanes (3D). We derive the hyperplane coefficients using the whole-brain data, although we exclude certain voxels that are likely to be outliers. First, we exclude voxels with a T1 value higher than 2 s to exclude CSF voxels⁴⁷. Second, we exclude voxels with transmit-coil inhomogeneity values more than two s.d. from the mean transmit-coil values. Using the fitted polynomial, we interpolate the transmit-coil inhomogeneity estimates to the high-resolution spoiled-GE. Regions in the high-resolution spoiled-GE that are not covered by the low-resolution bias map are estimated by extrapolation using a second-order 3D polynomial that spans the target volume.

We use the estimated transmit-coil inhomogeneity and the several flip-angle spoiled-GE measurements to derive the high-resolution T1 and M_0 maps. These were calculated using a nonlinear least-squares (NLS) fitting procedure⁴⁸ to minimize the difference between the data and the signal equation predictions (equation (3)).

Proton density mapping–receive coil inhomogeneity correction. At each point in the volume, PD is proportional to M_0 . But the M_0 data are contaminated with T2* decay and receive-coil imperfections and an arbitrary instrument-scaling factor (see equation (4)). For short TE measurements, the T2* decay can be neglected. Hence, the main challenge we face is removal of the receive-coil inhomogeneity.

We estimated the receive-coil inhomogeneity by combining data obtained from the individual coil elements. Just as in parallel imaging algorithms, the estimation procedure relies on the fact that multiple coils measure the same PD but with different coil gains. The estimation algorithm is described as below.

The brain image was gridded into a set of partially overlapping volumes, each approximately 20 mm³ with 50% overlap of neighboring volumes. The volumes were processed independently. For the i th coil, we estimated $M_{0,i}(\alpha)$ from the measured signal $S_i(\alpha)$ and the estimated T1 map and the corrected α (above) using equation (5):

$$M_{0,i}(\alpha) = \left(\frac{S_i(\alpha)(1 - \cos(\alpha)e^{-\frac{TR}{T1}})}{\sin(\alpha)(1 - e^{-\frac{TR}{T1}})} \right) \quad (5)$$

We use the average of these estimates over α as the mean $M_{0,i}$ for that volume and coil. We assumed that within each volume the gain (g_i) is a third-order polynomial spanning the volume^{39,40,49}. The fitting procedure is constrained to assume that all $M_{0,i}$ images share the same PD component. From g_i and $M_{0,i}$, each coil estimates a PD_i (equation (4)). We solve for the polynomials g_i that produce the greatest agreement between the PD_i estimates from the different coils:

$$\min_{g_i} \left\{ \sum (PD_i - \overline{PD}_i)^2 \right\} \quad (6)$$

To regularize the search across the polynomial coefficients, we further require that the correlations between the g_i do not exceed the correlations between $M_{0,i}$ and $g_i > 0$.

The last step is to combine the \overline{PD} maps estimated from each of the gridded estimation volumes. We set the mean in overlapping volumes to be equal and then average the measures across volumes.

Volume calculations. We derive the water volume and macromolecular tissue volume (WV and MTV) in each voxel from the PD map. We use the calculated PD values in CSF as a baseline to indicate a voxel with only water. Hence, to derive the fraction of the voxel volume that is water, we normalize the map by the mean value from a region of interest (ROI) in the cerebrospinal fluid (CSF). The CSF was identified using the FreeSurfer segmentation algorithm⁹ and was limited to voxels with a T1 in the range 4–5 s (ref. 50). Aside from water, the molecules present in CSF are in relatively low concentration, so we assume the normalized measured water fraction is reasonable. The normalized PD values are between 0 and 1, and the few locations >1 are clipped. These normalized PD maps measure water volume fraction (WVF) in each voxel. The macromolecular tissue volume fraction (MTVF) is $1 - \text{WVF}$, and both can be expressed in volume units when we multiply the fraction by the voxel volume.

Map reliability. Phantom. A homogenous agar phantom was used to evaluate the quality of the RF-coil inhomogeneity correction. To estimate the RF-excite homogeneity, we measured the T1 using SEIR-epi. We compared the phantom T1 map using SEIR-epi with a gold standard SEIR⁴⁷.

To evaluate the receive-coil homogeneity correction, we measured the PD values in the homogenous phantom. The s.d. of the PD values measures the reliability of the receive-coil measurements.

Human. To measure the T1 estimation error, one of the subjects was scanned 12 times at 1.5 T with a large set of flip angles ($\alpha = 4^\circ, 10^\circ, 20^\circ, 30^\circ, 20^\circ, 10^\circ, 4^\circ, 10^\circ, 20^\circ, 30^\circ, 4^\circ, 20^\circ, 4^\circ, 10^\circ$ and 30°) and 2-mm^3 voxel size using the same TR and TE. We performed a bootstrap analysis of these scans, randomly selecting a set of flip angles ($4^\circ, 10^\circ, 20^\circ$ and 30°) in a thousand repeats to estimate the T1 map using a linear approximation¹⁹. The T1 estimation error was defined as the s.d. of the estimated T1 values.

To further characterize the effect of flip angles, the same subject was scanned with slightly different flip angles ($3^\circ, 5^\circ, 9^\circ, 11^\circ, 18^\circ, 22^\circ, 26^\circ$ and 4°). The T1 value was estimated again with a set of values higher ($5^\circ, 11^\circ, 22^\circ$ and 34°) and lower ($3^\circ, 9^\circ, 18^\circ$ and 26°) than the standard flip-angle set. The estimated T1 values from these two sets were compared to the T1 values derived from the standard flip-angle set.

To characterize the effects of TR and TE on the estimation, another subject was scanned at 1.5 T using TR = 20 ms and 80 ms, TE 2 and 12 ms and $\alpha = 4^\circ$ and 18° , with voxel size = 2 mm^3 .

To estimate the reliability and generalization of the maps in humans, we performed multiple scans on different scanners using the parameters listed above. To estimate reliability within instruments, two subjects had three measurements in the same 1.5-T scanner and two subjects were scanned twice in the same 3 T scanner using different receive coils. To estimate reliability across instruments, two subjects had two measurements in two different 1.5-T scanners, and two subjects had two measurements in two different 3-T scanners. Three of the subjects scanned at the 1.5-T scanner were also scanned at a 3-T scanner.

Additional MR methods. Data alignment. We either collected high-resolution T1-weighted anatomical images for each subject using an 8-min sagittal 3D spoiled-GE sequence (1 mm^3 voxel size) or synthesized an equivalent T1-weighted image from the accrued acquired multi-flip-angle spoiled-GE

images⁵¹. For alignment, several anatomical landmarks were manually defined in the T1 images: the anterior commissure (AC), the posterior commissure (PC) and the midsagittal plane. Using these landmarks, we calculated a rigid-body transform to convert the T1-weighted images to the conventional AC-PC aligned space. This T1-weighted image was then used as a common reference for alignment of the T1, PD, MTV, VIP, MT and DTI maps.

Co-registration of multiple scans of the same subject. When brain volumes from the same subject were compared, the two volumes were coregistered using affine transformations determined using semi-automatic procedures with cubic interpolation implemented with in-house software.

0.5-T T1 mapping. Two subjects were scanned at a 0.5-T GE Signa SP with a quadrature head coil. The spoiled-GE parameter was similar to the one in 1.5 T and 3 T. The scan resolution at 0.5 T was $1.5 \times 1.5 \times 3\text{ mm}^3$. At 0.5 T, the T1 data were acquired using a combined transmit-receive quadrature head coil. On this instrument, the multicoil images and the specific SEIR-epi sequence used for transmit correction are not available. Hence, the coil corrections applied to the 1.5 T and 3 T data is not applicable at this low field strength. In this case, we assume that there is minimal transmit-coil inhomogeneity. These data were used only for comparison of T1 values at different field strengths.

T1 estimation with spin-echo inversion recovery (gold standard). Two subjects in 1.5 T and four subjects at 3 T were scanned with these parameters: one to three slices were acquired using the SEIR sequence, a receive-only head coil and the following parameters: TR = 2550 ms, TE = 10 ms, TI = 50, 400, 1,100 and 2,500 ms, BW = $\pm 32\text{ kHz}$, FOV = $24 \times 18\text{ cm}^2$ and slice thickness = 5 mm (ref. 47).

Magnetization transfer measurements. For five of the subjects, the T1 mapping procedure was followed by magnetization transfer spoiled-GE scans with variable offset frequency (TR = 32 ms, TE = 2.4 ms, $\alpha = 10^\circ$, $\Delta = 3, 6, 9$ or 12 kHz)⁵².

Fluid-attenuated inversion recovery. We collected fluid-attenuated inversion recovery (FLAIR) scans from each of the patients with multiple sclerosis (TR = 8 s, TE = 129 ms, inversion time = 2,250 ms, inplane resolution = 0.43 mm^2 and slice thickness = 5 mm).

Diffusion tensor imaging and tractography. Whole-brain DTI measurements were performed using a diffusion-weighted spin-echo EPI sequence with isotropic 2-mm^3 resolution. We measured 96 diffusion directions with a b value of $2.0\text{ ms per } \mu\text{m}^2$ and eight repeats of the same sequence with no diffusion weighting. We used $2.5 \times$ ASSET acceleration to reduce EPI distortions.

Fiber tracts were estimated using a deterministic streamlined tracking algorithm^{53,54}. The methods are described in detail elsewhere^{24,55}. The tracts were identified in each individual by restricting fibers to two waypoint ROIs (shown in Fig. 4a) that were defined based on a DTI atlas of human white matter⁵⁶.

For both fiber tracts of interest in this study, tractography algorithms estimated a dense set of core pathways along with a small proportion of pathways that are outliers. To minimize the influence of the outliers, we combine data from different voxels in a weighted fashion, assigning greater weight to voxels near the core of the estimated tract⁵⁷.

The algorithm for calculating the weights is the following. All fibers were clipped to the portion spanning the two waypoint ROIs such that each fiber was approximately the same length. Then the fiber groups were resampled to equal numbers of nodes; in this case we used 50 nodes along the track. We computed the mean position of each of the 50 nodes and defined this as the fiber tract core. We specified the diffusion at each node of the fiber group core as a weighted average of the diffusion measured near the equivalent node of each individual fiber in the group. The contribution of a given fiber is weighted by its distance from the tract core. We measure the distance from the node to a voxel using the covariance matrix of the node position. Specifically, if a voxel position is X , the mean position is X_0 , and the covariance matrix of the 3D node position is C , then we calculate the Mahalanobis distance, d , as follows:

$$d = \sqrt{(X - X_0)^T C^{-1} (X - X_0)} \quad (7)$$

The weight assigned to data from a voxel is the inverse of its distance, d . This procedure assigns higher weights to fibers near the bundle core as describe in detail by Yeatman *et al.*²⁸.

41. Koenig, B.W. & Gawrisch, K. Specific volumes of unsaturated phosphatidylcholines in the liquid crystalline lamellar phase. *Biochim. Biophys. Acta* **1715**, 65–70 (2005).
42. Loosley-Millman, M.E., Rand, R.P. & Parsegian, V.A. Effects of monovalent ion binding and screening on measured electrostatic forces between charged phospholipid bilayers. *Biophys. J.* **40**, 221–232 (1982).
43. Ulrich, A.S. & Watts, A. Molecular response of the lipid headgroup to bilayer hydration monitored by 2H-NMR. *Biophys. J.* **66**, 1441–1449 (1994).
44. Nagle, J.F. Theory of the main lipid bilayer phase transition. *Annu. Rev. Phys. Chem.* **31**, 157–196 (1980).
45. Polman, C.H. *et al.* Diagnostic criteria for multiple sclerosis: 2005 revisions to the “McDonald Criteria”. *Ann. Neurol.* **58**, 840–846 (2005).
46. Kurtzke, J.F. Rating neurologic impairment in multiple sclerosis: an expanded disability status scale (EDSS). *Neurology* **33**, 1444–1452 (1983).
47. Barral, J.K. *et al.* A robust methodology for *in vivo* T1 mapping. *Magn. Reson. Med.* **64**, 1057–1067 (2010).
48. Chang, L.C., Koay, C.G., Basser, P.J. & Pierpaoli, C. Linear least-squares method for unbiased estimation of T1 from SPGR signals. *Magn. Reson. Med.* **60**, 496–501 (2008).
49. Dale, A.M., Fischl, B. & Sereno, M.I. Cortical surface-based analysis. I. Segmentation and surface reconstruction. *Neuroimage* **9**, 179–194 (1999).
50. Hopkins, A.L., Yeung, H.N. & Bratton, C.B. Multiple field strength *in vivo* T1 and T2 for cerebrospinal fluid protons. *Magn. Reson. Med.* **3**, 303–311 (1986).
51. Sigalovsky, I.S., Fischl, B. & Melcher, J.R. Mapping an intrinsic MR property of gray matter in auditory cortex of living humans: a possible marker for primary cortex and hemispheric differences. *Neuroimage* **32**, 1524–1537 (2006).
52. Yarnykh, V.L. & Yuan, C. Cross-relaxation imaging reveals detailed anatomy of white matter fiber tracts in the human brain. *Neuroimage* **23**, 409–424 (2004).
53. Basser, P.J., Pajevic, S., Pierpaoli, C., Duda, J. & Aldroubi, A. *In vivo* fiber tractography using DT-MRI data. *Magn. Reson. Med.* **44**, 625–632 (2000).
54. Mori, S., Crain, B.J., Chacko, V.P. & van Zijl, P.C. Three-dimensional tracking of axonal projections in the brain by magnetic resonance imaging. *Ann. Neurol.* **45**, 265–269 (1999).
55. Dougherty, R.F., Ben-Shachar, M., Bammer, R., Brewer, A.A. & Wandell, B.A. Functional organization of human occipital-callosal fiber tracts. *Proc. Natl. Acad. Sci. USA* **102**, 7350–7355 (2005).
56. Wakana, S., Jiang, H., Nagae-Poetscher, L.M., van Zijl, P.C. & Mori, S. Fiber tract-based atlas of human white matter anatomy. *Radiology* **230**, 77–87 (2004).
57. Corouge, I., Gouttard, S. & Gerig, G. A statistical shape model of individual fiber tracts extracted from diffusion tensor MRI. *Lect. Notes Comput. Sci.* **3217**, 671–679 (2004).